

Contents lists available at ScienceDirect

# Solar Energy

journal homepage: www.elsevier.com/locate/solener



# A numerical and experimental study of a cellular passive solar façade system for building thermal control



Gert Guldentops, Steven Van Dessel\*

Architectural Engineering Program, CEE Department, Worcester Polytechnic Institute, 100 Institute Rd, 01609 Worcester, MA, United States

#### ARTICLE INFO

Article history: Received 14 April 2016 Received in revised form 1 March 2017 Accepted 27 March 2017 Available online 11 April 2017

Keywords:
Passive thermal control
Cellular facade
Phase change material
Finite element analysis

#### ABSTRACT

About 39% of total energy in the United States is consumed in residential and commercial buildings. Passive Solar Design (PSD) strategies have been successful in reducing building energy consumption, however, they require a substantial design effort for each individual project and are also difficult to implement in building retrofit projects. These characteristics tend to inhibit the widespread use of PSD principles in buildings today. In this paper a building envelop system is presented that incorporates small air cells backed by phase change material. The goal is to achieve quasi-constant core temperatures within a building enclosure system. The proposed technology results in a cladding system that can be used to thermally condition buildings. Initial experimental and numerical research efforts show that the system has significant potential to function properly when exposed to winter conditions. While initial results are promising, the system will require dynamic response to function properly in both winter and summer conditions.

© 2017 Elsevier Ltd. All rights reserved.

# 1. Introduction

Energy consumption in residential and commercial buildings currently stands at about 39% of total energy consumption in the United States (Berry and Michaels, 2012). PSD (Passive Solar Design) strategies, operating at whole building scale, seek to reduce building energy consumption by balancing heat transfer across the building envelope with solar energy input, while also using thermal mass and/or ventilation to dampen diurnal external influences (Sadineni et al., 2011). PSD has been used in buildings ranging in size from small-scale residential projects to large-scale multistory buildings (Kruzner et al., 2013; Samuel et al., 2013), and the approach has been shown applicable to different climate types (Ralegaonkar and Gupta, 2010). PSD strategies are however highly sensitive to meteorological factors and thus require a thorough understanding of climatic factors and the use of building energy simulation tools (Ralegaonkar and Gupta, 2010; Stevanovi, 2013). It is also difficult to implement PSD strategies into older existing buildings, which are responsible for the bulk of building-related energy expenditures both globally and in the US (Stevanovi, 2013) These characteristics tend to inhibit the widespread use of traditional PSD principles in buildings today (Sadineni et al., 2011).

The past decades have also seen steady development of various technologies aimed at applying PSD at the scale of the building envelope. Some notable examples include Trombe walls (Saadatian et al., 2012), transparent insulation systems (Kaushika and Sumathy, 2003; Sharma and Kaushika, 1987; Wallner et al., 2006; Cadafalch and Cònsul, 2014), double skin façades (Shameri et al., 2011; Gratia and De Herde, 2004; Fallahi et al., 2010), ASTF (Active Solar Thermal Facades) (Ma et al., 2015), and PCM (Phase Change Material) (Kuznik et al., 2011). A Trombe wall can reduce building energy usage up to 30% (Hordeski, 2004). However, Trombe walls suffer from two key shortcomings. Trombe walls have low thermal resistance, causing a negative heat flux during prolonged cloudy periods (Chan et al., 2010; Shen et al., 2007; Zamora and Kaiser, 2009), and they are also difficult to control due to the unpredictable nature of the weather (Chan et al., 2010; Onbasioglu and Egrican, 2002). Transparent insulation combines the advantages of opaque insulation with solar collection (Kaushika and Sumathy, 2003; Sharma and Kaushika, 1987). This was initially used as convection suppressant devices to improve the efficiency of solar energy collectors (Francia, 1961; Veinberg and Veinberg, 1959), although lacks a mechanism to control the thermodynamics of the building envelope. Multiple ASTF systems have also been tested, some of which are an adaptation of traditional double skin façade systems. Most can be categorized as Building Integrated Solar Thermal, Building Integrated Photovoltaic, or a combination thereof. The active component lowers

<sup>\*</sup> Corresponding author.

E-mail address: svandessel@wpi.edu (S. Van Dessel).

#### Nomenclature surface absorptivity radiative intensity $\Delta T_{pc}$ phase transition temperature range $I(\Omega)$ radiative intensity at angle $\Omega$ к attenuation coefficient radiosity wavelength k thermal conductivity λ dynamic viscosity air cell length μ $l_{cell}$ density latent heat capacity Σ building enclosure tilt angle Ν opaque sky cover pressure g gravitational constant velocity, vector RH relative humidity 11 3 surface emissivity Т temperature surface azimuth angle time 0 specular solar irradiance on a horizontal plane average air cell temperature $B_{sol,h}$ $T_{a,cell}$ specific heat capacity $T_{a,ext}$ external air temperature $c_p$ $T_{a,int}$ apparent heat capacity internal air temperature $c_{p,app}$ air cell diameter thickness external cover plate $d_{cell}$ $t_{cover}$ diffuse solar irradiance on a horizontal plane $T_{dp}$ $D_{sol,h}$ dewpoint temperature blackbody hemispherical emissive power thickness insulation backing $e_b(T)$ $t_{ins}$ $T_{pcm}$ irradiance average PCM temperature $G_m$ mutual irradiation between different exposed surfaces $T_{pc}$ phase transition temperature $G_{sol}$ solar irradiance $T_{skv}$ sky radiative temperature external surface forced heat transfer coefficient temperature of surrounding surfaces $T_{sur}$ $h_{ext,f}$ $h_{ext,n}$ external surface natural heat transfer coefficient wind velocity, scalar $\nu_{\rm w}$ $h_{ext}$ external surface heat transfer coefficient wind direction internal surface heat transfer coefficient $h_{int}$ Height internal ceiling height

the incident solar gains, thus decreasing building cooling loads (Lai and Hokoi, 2015; Quesada et al., 2012a,b). Building integrated solar energy collectors however suffer from integration issues (Buker and Riffat, 2015) that lead to high cost and relatively low system efficiency (Quesada et al., 2012b).

PCM is often employed within PSD systems to buffer solar energy, allowing for a more efficient bridging of periods with low solar insolation (Baetens et al., 2010; de Gracia et al., 2015; Boukhris et al., 2009). The most common categories of PCM are: (i) organic compounds, such as paraffins and fatty acids, (ii) inorganics, like hydrated salts, and (iii) eutectics and their mixtures (Tatsidjodoung et al., 2013). Organic PCMs tend to have the advantage of being none-corrosives, low to no subcooling, low thermal conductivity, and long-term chemical and thermal stability, which is in contrast with inorganic PCMs. The advantage of inorganic PCMs is the greater phase change enthalpy (350  $\frac{\text{MJ}}{\text{m}^3}$ ) over organic PCMs (150  $\frac{\text{MJ}}{\text{MJ}}$ ) (Cabeza et al., 2011).

Various solutions have been developed to improve the performance of passive solar systems (Wallner et al., 2005a,b). Notable is the development of low-e (low emittance) coatings (Cuce and Riffat, 2015; Ebisawa and Ando, 1998), with a typical emissivity of 0.04 (Ebisawa and Ando, 1998) to 0.18 (Schaefer et al., 1997). However, solar spectrum transmittance of low-e coatings tends to fall between 0.60 and 0.75, which is a key drawback when harvesting solar energy. In ongoing solar energy collector research, AZO (Aluminum-doped Zinc Oxide) and ITO (Tin-doped Indium Oxide) coatings are optimized for such applications (Al-Mahdouri et al., 2014; Giovannetti et al., 2012). Total emissivities between 0.20 and 0.30 have been reported in combination with a solar transmittance of 0.85 or higher. An AR (Anti-Reflective) coating (Chen, 2001; Rosencrantz et al., 2005; Hammarberg and Roos, 2003) with a low refractive index is, however, necessary in combination with the AZO or ITO coatings in order to obtain such a performance (Giovannetti et al., 2012).

This study is an investigation into the application of solar energy harvesting in combination with PCM at the mm to cm scale,

rather than the whole building or building envelope scale. The system under consideration is composed of small cellular air pockets with transparent front-cover, which convert solar irradiance into heat, backed by the heat buffering capacity of PCM pockets (see Fig. 1). The energy harvesting effect within the system is regulated by the application of opaque walls in between the air cells, causing a more shallow penetration of solar radiation during summer conditions compared to winter conditions. The solar energy admittance rate and energy loses are further regulated using various coatings applied to the system. Choosing a specific cell geometry that optimizes the convective flow within, and thus optimizing heat transfer from the air cell towards the external environment.

With sufficient heat capacity (sensible or latent) and control features it becomes possible to minimize the heat flux across the building envelope, and thus realize a passive zero-energy building enclosure system.

The research goals of this paper are to: (i) investigate the impact of certain system parameters on the behavior of the system, such as cell geometry, properties of the PCM, and the application of coatings on the external cover, and (ii) to investigate what shortcomings can be observed.

A numerical modeling framework is presented (Section 2) to investigate the sensitivity of these parameters. Experiments have been carried out to help investigate system behavior, and to validate the numerical model (Section 3). A parametric study was performed to fulfill these research goals (Section 5). We conclude by describing general behavior of the system and its potential for further development (Section 7).

## 2. Finite element modeling

A numerical model has been developed to investigate the potential of the proposed cellular façade concept. A simplified 2D geometry is used to reduce complexity. A schematic of the geometry and mesh are depicted in Fig. 2.

The necessary weather parameters to run the model are external air temperature,  $T_{a,\text{ext}}$ , relative humidity, RH, wind velocity,  $v_w$ ,

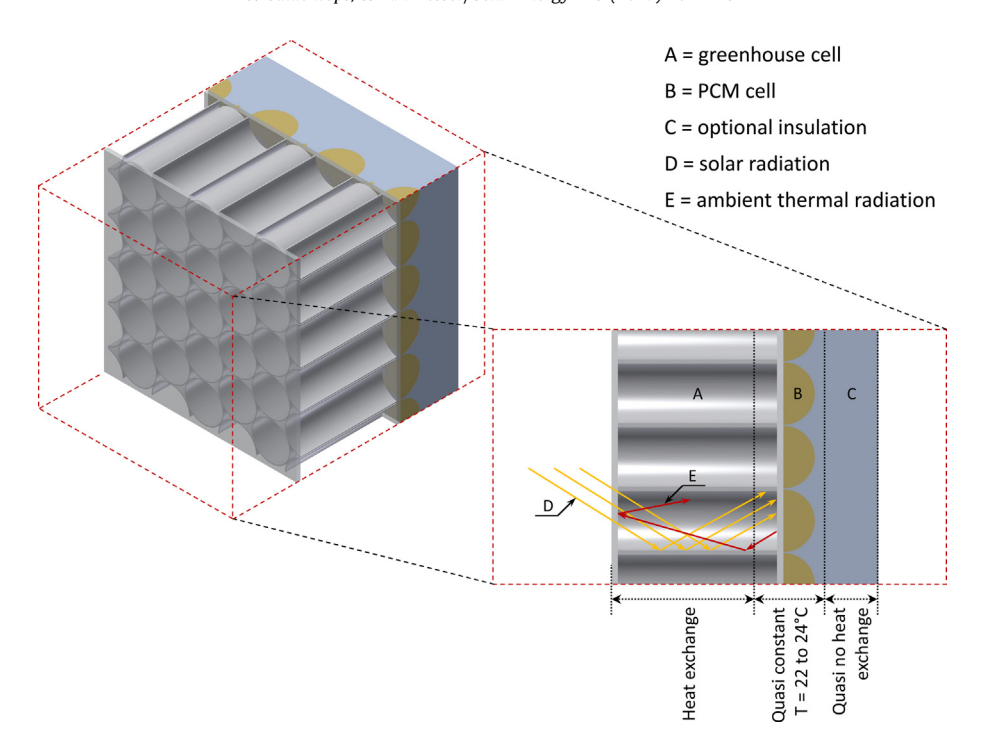


Fig. 1. Schematic overview of the proposed concept.

direction,  $v_d$ , and both specular,  $B_{sol,h}$ , and diffuse,  $D_{sol,h}$ , solar irradiance on a horizontal plane. The final necessary weather parameter is the opaque sky cover, N, clear sky (N=0), complete overcast (N=1), expressed in tenths. Geographic location and orientation of the system are also required.

# 2.1. Governing equations

The governing equations employed by the numerical model are the heat equation (Eq. (1)) in combination with the Navier-Stokes equation (Eq. (2)), and the continuity equation (Eq. (3)) (Bergman et al., 2011), as follows:

$$\rho c_p \left[ \frac{\partial T}{\partial t} + (\mathbf{u} \cdot \nabla) T \right] = \nabla (k \nabla T) + \nabla \cdot q_r \tag{1}$$

$$\frac{\partial \mathbf{u}}{\partial t} + \rho (\mathbf{u} \cdot \nabla) \mathbf{u} = \nabla [-p + \mu \nabla \mathbf{u}] - \rho \mathbf{g} \tag{2}$$

$$\frac{\partial \rho}{\partial t} + \rho \nabla(\mathbf{u}) = 0 \tag{3}$$

A laminar flow regime is assumed here. In the solid domains only a reduced form of the heat equation is solved for. The PCM is assumed not to exhibit a significant flow regime. Required here are the following material properties: density,  $\rho$ , specific heat

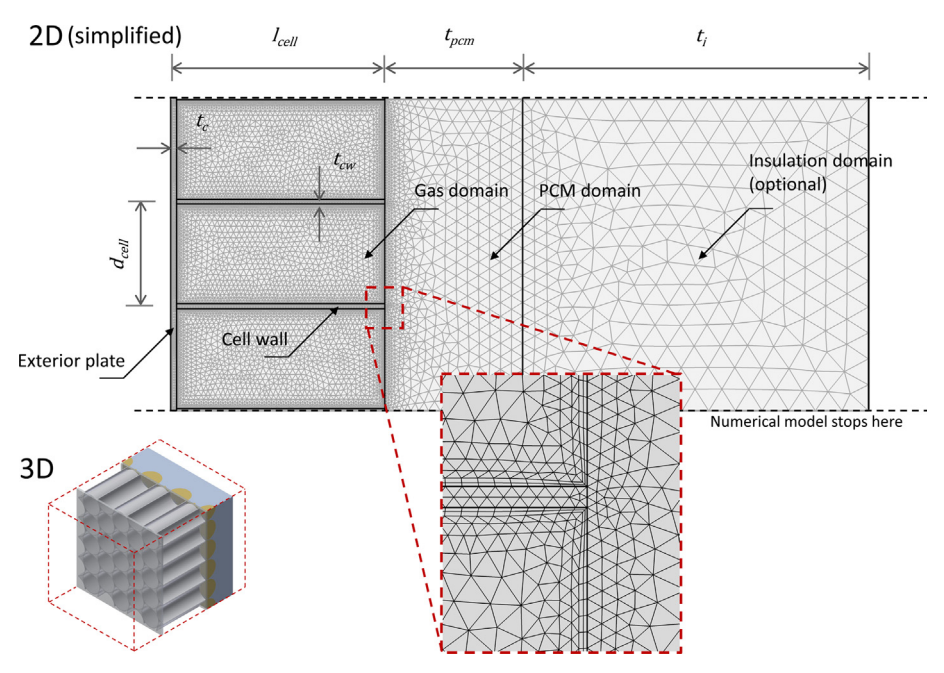


Fig. 2. Geometric overview of the FE model and corresponding mesh.

capacity,  $c_p$ , thermal conductivity, k, and the dynamic viscosity,  $\mu$ . In Navier-Stokes,  $\mathbf{u}$  is the flow velocity vector, p is pressure, and  $\mathbf{g}$  is the gravitational constant.

Solid domains transparent to solar radiation are assumed to absorb some radiation within the medium. In order to take this into account, a radiation in participating media (Eq. (4)) is added to the model. This equation is based on the Lambert-Beer law (Howell et al., 2016). Here,  $\kappa$  is the attenuation coefficient, and  $I(\Omega)$  is the radiative intensity at angle  $\Omega$ .

$$\nabla \cdot q_r = \int_{\Omega = 0}^{\pi} -\kappa I(\Omega) \, d\Omega \tag{4}$$

The PCM domain contains a modified heat capacity value in order to incorporate the effect of phase transition. This apparent heat capacity ( $c_{p,app}$ ), is defined as follows:

$$c_{n,ann} = c_n(T) + LH(T) \tag{5}$$

The effect of latent heat capacity is incorporated into the model using Eq. (6), where LH stands for latent heat capacity, and  $\frac{(dz_{m})}{dT}$  is a Dirac pulse. This gradient is introduced to allow for a gradual phase transition over a specified temperature interval  $(\Delta T_{pc})$ . This equation is evaluated separately for each finite element used in the model.

$$LH(T) = LH\frac{d\alpha_m}{dT} \tag{6}$$

The hysteresis effect associated with phase transitions is incorporated in the model by using separate enthalpy curves (Eq. (6)) for melting and solidifying. A binary phase indicator is evaluated for all the elements, at all time steps. After a complete phase transition, the value of this indicator changes, allowing for the use of the appropriate enthalpy curve.

The FE modeling framework utilizes, two spectral bands (solar radiation  $0.25~\mu m < \lambda < 2.5~\mu m$ , and IR radiation,  $\lambda \geqslant 2.5~\mu m$ ). Optical properties are assumed independent of wavelength within each bandwidth.

The solar radiation impinging on the exterior cover plate of the system,  $G_{sol}^{\Omega} = \int_{\lambda=250}^{2500} \text{nm} G_{sol}(\lambda,\Omega) d\lambda$ , is modeled as an external radiation source (Hutcheon and Handegord, 1995). The power of the specular solar irradiance component,  $B_{sol}(\Omega)$ , on the external surface of the building enclosure is calculated as a function of the intensity on a horizontal plane,  $B_{sol,h}$ , the solar zenith angle, and solar incidence angle. These angles are calculated using equations reported by Meeus (1991). The power of the diffuse component,  $D_{sol}(\Omega)$ , on the external surface is calculated using an experimentally based model developed by Perez et al. (1987, 1988), which factors in surface orientation and sky conditions. Radiation received by surfaces in the vicinity of the building enclosure is assumed to be partially and diffusely reflected, and subsequently received by the building enclosure surface (Hutcheon and Handegord, 1995).

# 2.2. Boundary conditions

The surface reflection of solar radiation on both the front and back surface of the external cover plate is calculated based on Snell's law and the Fresnel equations (Quimby, 2006). Angle dependency of solar irradiance and solar surface reflectivity is, therefore, maintained for these two surfaces.

$$G_{sol} = \int_{\Omega=0}^{\pi} (1 - \alpha(\Omega)) [B_{sol}(\Omega) + D_{sol}(\Omega)] d\Omega$$
 (7)

Subsequent surface-to-surface radiation problems within the air cell, are solved using the radiosity method. Here, the radiative heat exchange is, by definition, the difference between incident

thermal radiation (irradiation, G) and the total radiation leaving the surface (radiosity, J). Or summarized: q'' = G - J. Surface properties are assumed independent of incidence angle and wavelength. Kirchhoffs law ( $\alpha_{\lambda} = \varepsilon_{\lambda}$ ) is also incorporated (Jones, 2000). Reflections of solar irradiance from the opaque cell walls are, therefore, assumed to be completely diffuse. The boundary condition equation for a surface-to-surface radiation problem, in which  $G_i$  at one point on the boundary is a function of  $J_i$  at every other point in view, is described as:

$$J_i = (1 - \alpha_i)[G_{m,i}(J_i) + G_{sol}] + \varepsilon_i e_b(T)$$
(8)

In Eq. (8), i refers to a specific spectral band and  $e_b(T)$  denotes the blackbody hemispherical emissive power.  $G_{m,i} = \int_{S'} \left[ \frac{(-\mathbf{n}'\cdot\mathbf{r})(\mathbf{n}\cdot\mathbf{r})}{\pi|\mathbf{r}|^4} \right] dS$  expresses the mutual irradiation between different exposed and meshed surfaces. The heat flux that arrives from element x' depends on the local radiosity J' projected onto element x (Howell et al., 2016). The projection is computed using the normal vectors  $\mathbf{n}$  and  $\mathbf{n}'$  along with the vector  $\mathbf{r}$ , which points from x to x'.

The internal cell walls also hold a no-slip temperature  $(T_{wall} = T_{fluid})$  and fluid velocity  $(v_{wall} = 0)$  boundary condition.

The external surface of the system, where it is under influence of the external diurnal conditions, requires a supplementary boundary condition (Eq. (9)). Since the external cover material can be assumed opaque to IR radiation, the Stefan-Boltzmann law is used to model this type of heat exchange. The external convective heat transfer is modeled using Newtons law of cooling.

$$-\mathbf{n} \cdot (-k\nabla T) = \varepsilon \sigma \left[ \left( \frac{1 + \cos \Sigma}{2} \right) (T_{\text{sky}}^4 - T^4) + \left( \frac{1 - \cos \Sigma}{2} \right) (T_{\text{sur}}^4 - T^4) \right] + h_{\text{ext}} (T_{\text{gext}} - T)$$
(9)

Models developed in Walton (1983) and Clark and Allen (1978) (Eqs. (10) and (11)) are used to estimate the sky radiative temperature,  $T_{sky}$ , which is used to calculate radiative heat exchange with the Earths atmosphere.

$$\epsilon_{sky} = \left(0.787 + 0.764 \ ln \left(\frac{T_{\textit{dp}}}{273}\right)\right) (1 + 0.0224 N - 0.0035 N^2 + 2.8 \cdot 10^{-4} N^3) \eqno(10)$$

$$T_{\text{sky}} = \left(\frac{\varepsilon_{\text{sky}} T_{a,\text{ext}}^4}{\sigma}\right)^{\frac{1}{4}} - 273.15 \tag{11}$$

Here, the dewpoint temperature,  $T_{dp}$ , expressed in Kelvin, can be estimated accurately based on RH and  $T_{a,ext}$  using a correlation found in Lawrence (2005). The temperature of the externally surrounding surfaces,  $T_{sur}$ , is assumed equal to  $T_{a,ext}$ .  $\Sigma$  denotes the enclosure tilt angle.

The external convective heat transfer,  $h_{ext}$ , used in Eq. (9), exists out of two distinct parts, the first being forced convection,  $h_{ext,n}$ , and the second being natural convection,  $h_{ext,n}$ .  $h_{ext,n}$  is derived using correlations that factor in surface-to-wind angle,  $w_d$ , and wind velocity,  $w_v$ , (Eq. (12)). These correlations have been derived using CFD tools (Emel et al., 2007) and have been validated using experimental data (Judkoff and Neymark, 1995). These do apply only for vertical or near vertical building enclosures.

$$h_{extf} = 5.15(w_v)^{0.81} \quad 0^{\circ} \le w_d < 22.5^{\circ}$$

$$h_{extf} = 3.34(w_v)^{0.84} \quad 22.5^{\circ} \le w_d < 67.5^{\circ}$$

$$h_{extf} = 4.78(w_v)^{0.71} \quad 67.5^{\circ} \le w_d < 112.5^{\circ}$$

$$h_{extf} = 4.05(w_v)^{0.77} \quad 112.5^{\circ} \le w_d < 157.5^{\circ}$$

$$h_{extf} = 3.54(w_v)^{0.76} \quad 157.5^{\circ} \le w_d < 180^{\circ}$$

 $h_{ext,n}$ , on the other hand, is determined based on a correlation (Eq. (13)) derived as a function of the temperature difference and surface orientation (Walton, 1983).

$$\begin{split} h_{\text{ext},n} &= \frac{9.482 |\Delta T|^{\frac{1}{3}}}{7.283 - |\cos \Sigma|} \quad \text{if } \Delta T < 0 \text{ upward, } \text{or} \Delta T > 0 \text{ downward} \\ h_{\text{ext},n} &= \frac{1.810 |\Delta T|^{\frac{1}{3}}}{1.382 + |\cos \Sigma|} \quad \text{if } \Delta T > 0 \text{ upward, } \text{or} \Delta T < 0 \text{ downward} \end{split}$$

The boundary at the interior side of the building enclosure is assigned Eq. (14), which is similar to Eq. (9). Here, however,  $T_{\infty}$ is assumed equal to the internal air temperature,  $T_{a.int}$ , for both the convective and IR radiative exchange. The internal convective heat transfer coefficient,  $h_{int}$ , is determined based on a correlation (Eq. (15)) derived using a large experimental test cell (Min et al., 1956). No forced convection is assumed here.

$$-\mathbf{n} \cdot (-k\nabla T) = \varepsilon \sigma(T_{a,int}^4 - T^4) + h_{int}(T_{a,int} - T)$$
(14)

$$-\mathbf{n} \cdot (-k\nabla T) = \varepsilon \sigma (T_{a,int}^4 - T^4) + h_{int}(T_{a,int} - T)$$

$$h_{int} = \frac{2(T_{a,int} - T_{int})^{0.32}}{Height^{0.04}}$$
(15)

The outer surfaces of the model, perpendicular to the external and internal boundaries, are assigned an adiabatic boundary condition,  $\frac{\partial T}{\partial n} = 0$ .

#### 2.3. Verification

In order to verify the FE modeling framework, a grid study has been performed. In our case, grid independence is achieved when using element sizes that range from 0.5 mm to 2.5 mm for the fluid inside the greenhouse cell, and 1 mm to 10 mm for the solid domains. A maximum time step of 2 min results in accurate interpolations of the solution in between time steps.

# 3. Experimental work

Experiments have been conducted to investigate the potential of the system, as well as validate the numerical model developed here. The experimental setup exists of single cell prototypes of the proposed system which were mounted in a large block of XPS insulation. The cell exists out of an air cell backed by a PCM cell. The block of XPS insulation was mounted in a southsoutheast facing window using a plywood frame that fits exactly in the window opening. This allows for the prototype to be exposed to the external diurnal weather cycles at the external cover, whilst having a nearly adiabatic boundary at the other cell boundaries. The experiment is summarized schematically in Fig. 3.

A minimum of 125 mm (5") of XPS insulation foam is applied around the prototypes to achieve the adiabatic boundaries and, in essence, separate the prototype from the interior environment of the building. This allows for a study of the system without the interference of any heat flux emanating from the interior environment of the building. Three different prototypes have been implemented, each of which has a unique cell diameter,  $(d_{cell} = 25 \text{ mm } (1''), 38 \text{ mm } (1.5''), and 51 \text{ mm } (2''))$ . The prototype cells are, however, equal in all other respects. The external cover of the prototype is made out of quartz glass  $(t_{cover} = 1.6 \text{ mm } (\frac{1}{16''}))$ , and thus allows for a high degree of solar transmittance. All other geometry parameters are summarized in Fig. 5. A Dimension SST 1200es rapid prototyping machine was used to manufacture the walls of both air and PCM cell.

The PCM used in these prototypes is organic in nature, and has a phase transition temperature of 22 °C and a latent heat capacity of 165  $\frac{1}{g}$  (Microtek Laboratories, Inc.). This is a colorless paraffin based PCM material with a relative density of 0.9. The exterior cover plate is made out of quartz glass with an overall transmissivity of 0.98 at the above specified thickness in the solar radiation spectrum. A reflectivity coefficient,  $\rho_{sol}$ , of the exterior glass surface is defined as a function of the angle of incidence of solar radiation,  $\theta_i$ , ranging from  $\rho_{sol}=0.04~@~\theta_i\leqslant 50^\circ$ , to  $0.3~@~\theta_i=80^\circ$ , and finally to 1.0 @  $\theta_i = 90^\circ$ . The cell walls are made out of black ABS plastic which is printed with complete infill (minimal air voids). An overview of the material properties is presented in Table 1 underneath (see Fig. 4).

Thermocouples, with I type calibration (Cole-Parmer), are inserted into the cell at various distances from the external cover. Thermocouple (TC) inserts are shown in Fig. 3. Fig. 5 depicts the location and label of each TC inserted within each cell. TC 1 is located in the greenhouse cell, whilst TC 2 and 3 register the PCM temperature, TC 4 measures temperature behind the PCM cell. The latter is the location where guasi-steady state ambient temperatures ( $\approx$  18 through 22  $^{\circ}$ C) are desired. A data logger (Campbell Scientific, CR1000) is used to capture the thermocouple readings.

Included in the setup is a small weather station (Davis Instruments, Vantage Pro2 Plus), which captures the external microclimate that surrounds the setup. Of interest here are  $T_{a,ext}$ , RH,  $w_v$ ,  $w_d$  and  $q''_{sol}$  measurements.

In the experimental data, the experimental data, it becomes clear the system is solar radiation driven. The proposed system can therefore perfectly function on cold days with a clear sky. A maximum temperature of 42 °C was reached in the air cell during the test period. Fig. 6 shows typical recorded system temperatures for the test period. The air cell reacts fast to changes in weather parameters, whilst the PCM reacts with significant latency, as can be expected.

The cells with a 51 mm (2'') diameter exhibits the highest average PCM temperature, although the 38 mm (1.5") diameter cell exhibits the highest peaks in PCM temperature. The 51 mm (2") diameter prototype cell could very well suffer from a higher degree of air leakage as it has more outer surface area and joint lengths. The 51 mm (2'') diameter cell also exhibits the lowest cooling rates after sunset, with the 38 mm (1.5") diameter cell cooling the fastest out of the three cells. The largest cell could benefit from more direct absorption of solar irradiance at the absorber surface, whilst the smallest cell probably benefits from some degree of internal convection suppression (see Fig. 7).

# 4. Model validation

A validation process has been completed and involved a comparison between the experimental thermocouple measurements and the numerical model, discussed in Sections 2 and 3 respectively. The geometry of the FEM model had to be slightly modified to match the experimental set-up. The underlying equations incorporated in the validated numerical model are, however, exactly as discussed in Section 2. The validity of this process should, therefore, still hold. Some components of the numerical model, such as the phase transition, have also been validated separately using benchmark models.

The experimental test period used for the validation process ran from January 27th through February 5th 2016, and contains both clear and (partially) cloudy periods. The solar irradiance measured by the weather station, is split into a diffuse and a specular part. This is achieved using the Perez direct/diffuse splitting model, which is explained at length in Perez et al. (1992).

A comparison between numerical and experimental data is presented in Figs. 8 and 9. The temperature of the air cell (TC 1, see Fig. 5) is depicted in Fig. 8. The average deviation between the

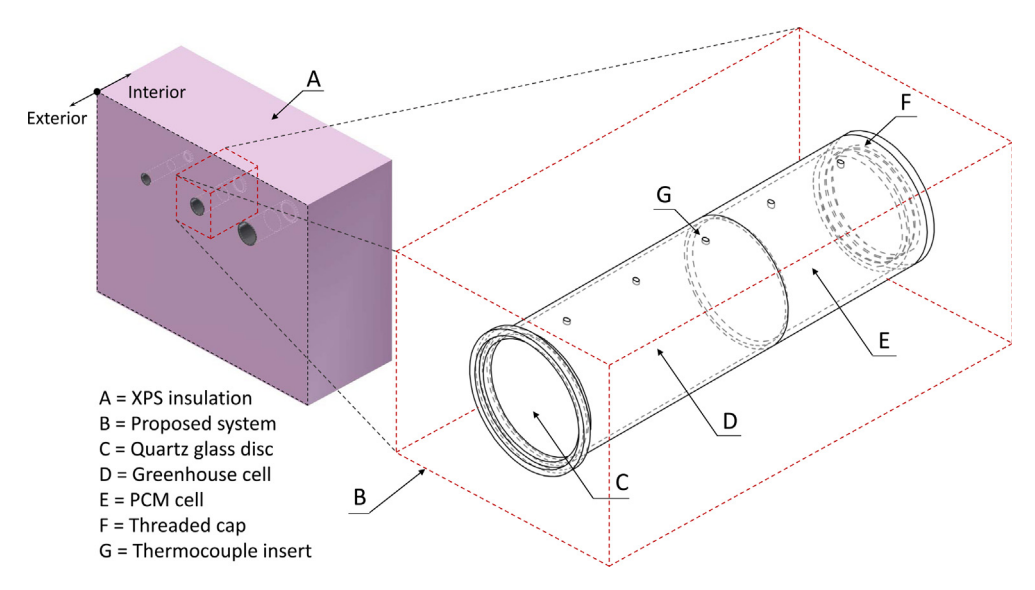


Fig. 3. Overview of the experimental setup.

**Table 1**Properties of materials used in experimental set-up.

Material	$k[\frac{W}{m\cdotK}]$	$C_p\left[\frac{\mathrm{kJ}}{\mathrm{kg}\cdot\mathrm{K}}\right]$	$ ho \left[ rac{\mathrm{kg}}{\mathrm{m}^3}  ight]$	α	$\mathcal{K}\big[\frac{1}{m}\big]$	$\epsilon$
ABS (black, 3D printed)	0.17	1420	1040	0.90		0.80
PCM (solid)	0.10	2800	900			
PCM (liquid)	0.10	2800	900			
Quartz glass	1.40	670	2200		12.4	0.70
White acrylic paint				0.20		0.90
XPS	0.034	1500	24.8			



Fig. 4. Interior and exterior picture of the experimental set-up.

numerical model and the experiment is 1.3 °C for the test period, with a maximum deviation of 4.0 °C. This for  $d_{cell}=38~\mathrm{mm}~(1.5'')$ . Slight inaccuracies in specular and diffuse irradiance levels, and the simplified 2D geometry probably explain these inaccuracies. From this it is possible to conclude that the air cell temperature is simulated with decent accuracy.

The thermocouples located within the PCM (TC 2 and 3, see Fig. 5), recorded, on average, slightly higher temperatures com-

pared to the simulation, although with a similar trend. Typical results for the comparison are shown in Fig. 9. An average deviation of 1.6 °C is observed over the test period regarding TC 2, with a maximum deviation of 7.5 °C for the case of the 38 mm (1.5") cell diameter. For TC 4, the average deviation increases to 2.0 °C. This for  $d_{cell} = 38$  mm (1.5"). The properties of the PCM, such as thermal conductivity are probably temperature dependent, a constant value probably leads to these increased inaccuracies. A slight devi-

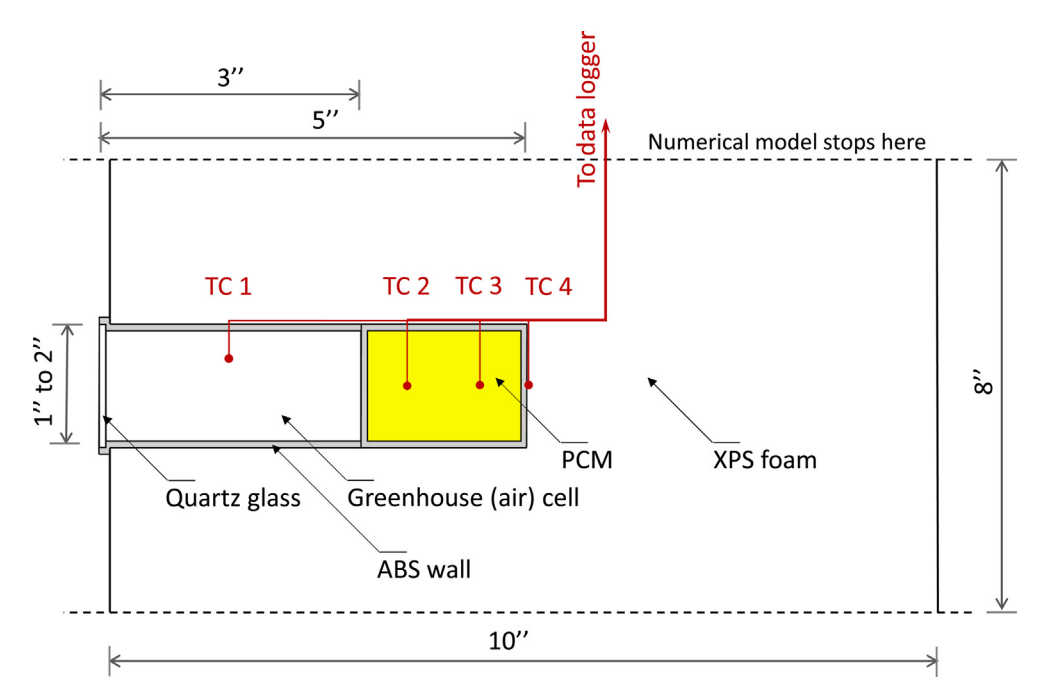


Fig. 5. Vertical cross section of the prototypes used for model validation, with location of thermocouples marked.

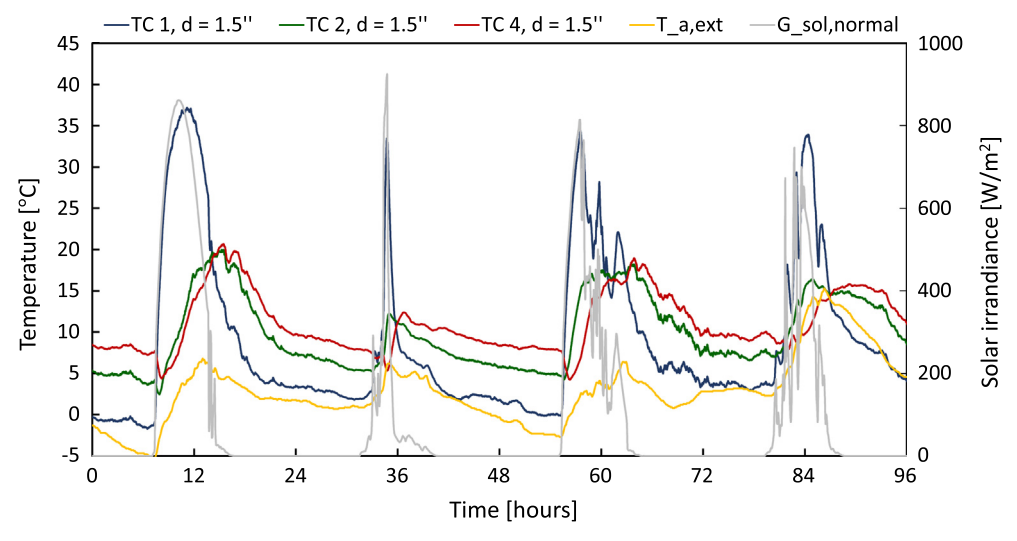


Fig. 6. TC 1, 2, and 4 for prototype,  $d_{cell} = 38 \text{ mm } (1.5'')$  as a function of time, as well as  $T_{a.ext}$  and  $G_{sol,normal}$ , January 31st through February 2nd.

ation between the intended and actual location of the thermocouple within the PCM could exist as well, which could lead to a significant difference in recorded temperatures. The model exhibits a better accuracy for  $d_{cell}=25~\mathrm{mm}~(1'')$ , as can be seen in Fig. 9, which can probably be explained by a lower degree of air infiltration for smaller  $d_{cell}$ .

## 5. Parametric study

A parametric study has been performed using the numerical model developed here. This will give us more insight in the heat transfer mechanisms occurring in the system, as well as potential consequences of these mechanisms on the heat transfer rate. Typical annual external weather conditions are generated using Meteonorm, which is based on historical central Massachusetts

weather data. The parametric study ranges from November 17th to December 1st for winter conditions, and from June 15th to June 28th for summer conditions.

# 5.1. Baseline

The baseline consists out of a system with an external cover made from low-iron glass, with a thickness of 3 mm ( $^18''$ ). The air cells are constructed using black ABS plastic with a 0.6 mm (0.025") wall thickness. The PCM ( $LH=180~\frac{kJ}{kg},k_{pcm}=0.5~\frac{W}{m\cdot K}$ ) has a melting temperature of 22°C and a solidifying temperature of 20°C, a 2°C hysteresis is therefore assumed. Any phase transition is assumed to occur over a 4°C temperature range. The system faces south ( $\varphi=0^\circ$ ), and is placed vertical ( $\Sigma=90^\circ$ ). The thickness of the PCM is limited to 25 mm (1").

<sup>1</sup> http://www.meteonorm.com.

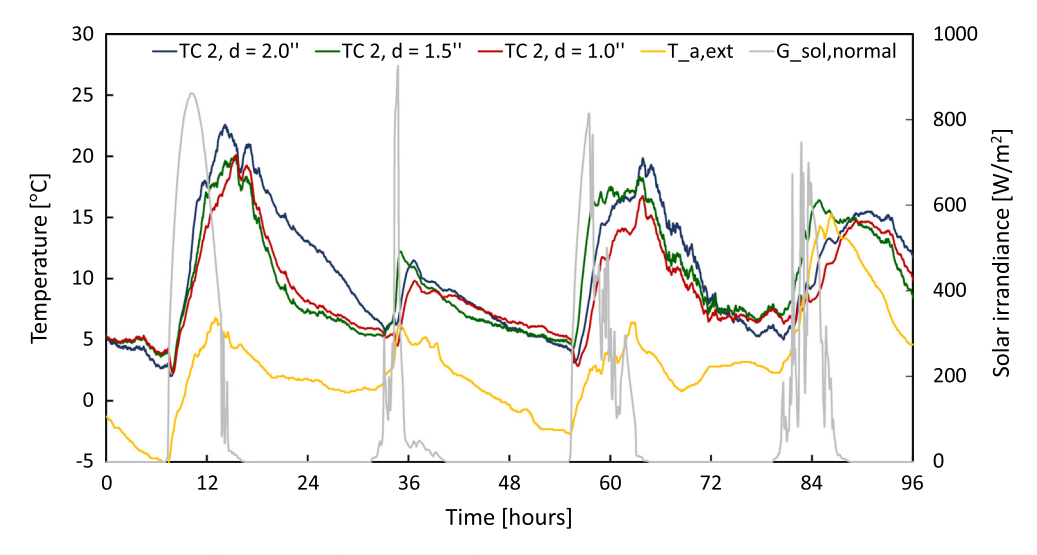
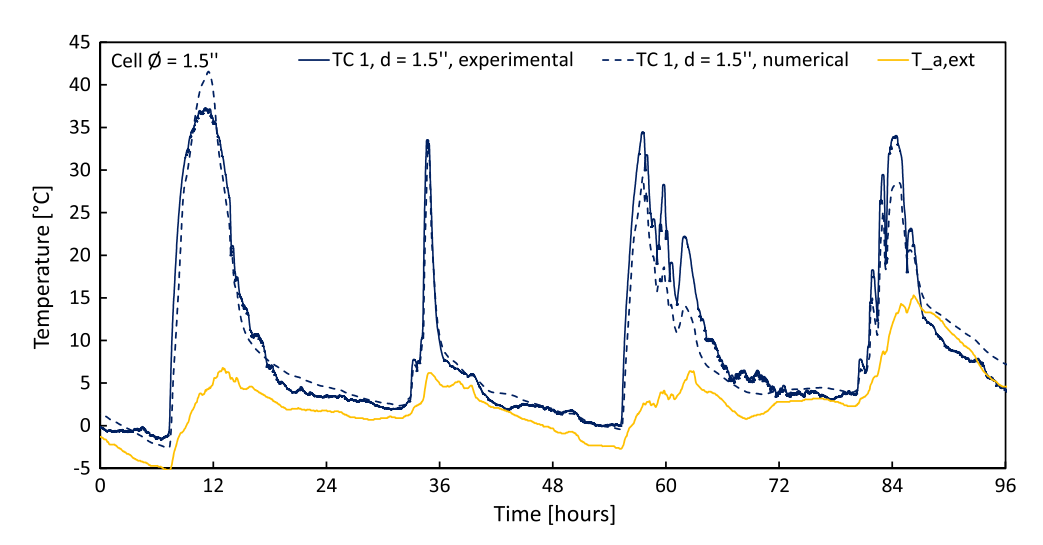


Fig. 7. TC 4 for all prototype,  $d_{cell} = 25 \text{ mm } (1'')$ , 38 mm (1.5'') and 51 mm (2'') as a function of time, as well as  $T_{a,ext}$  and  $G_{sol,normal}$ , January 31st through February 2nd.



**Fig. 8.** Comparison between experimental and numerical air cell temperature data (T1, see Fig. 5), for prototype with  $d_{cell} = 38 \text{ mm} (1.5'')$ .

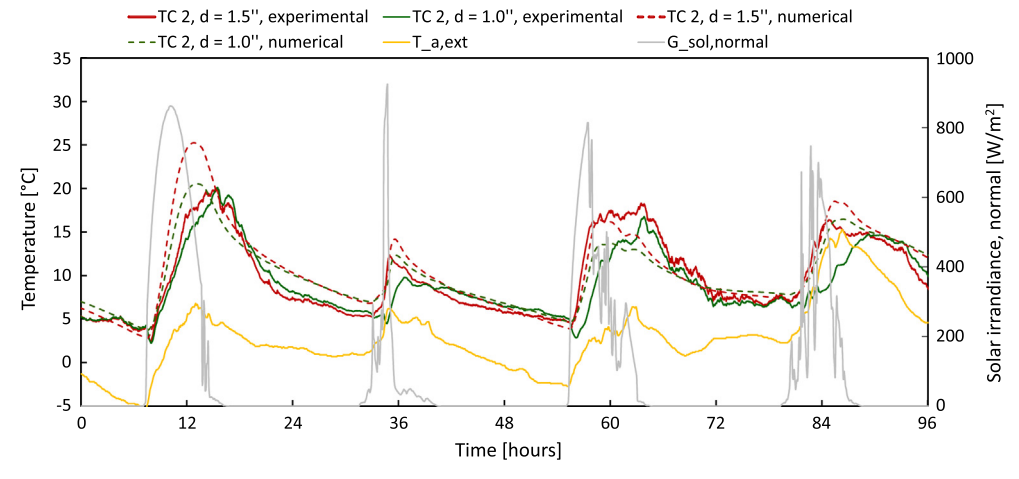
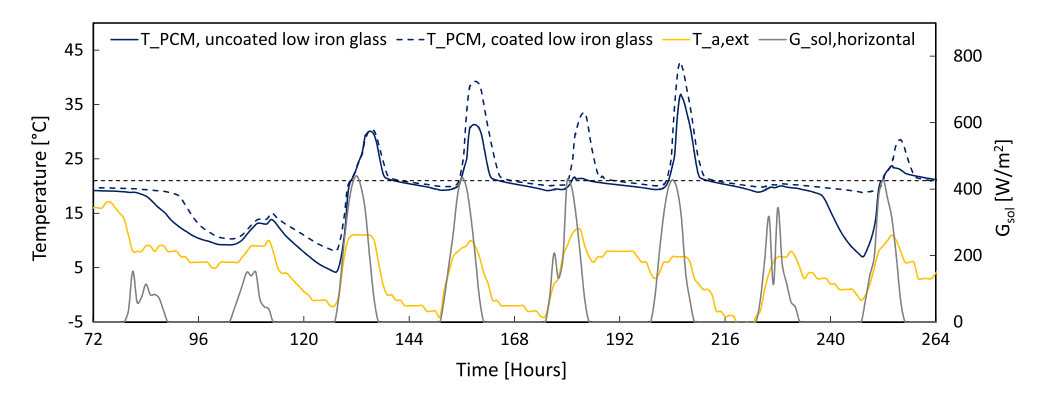
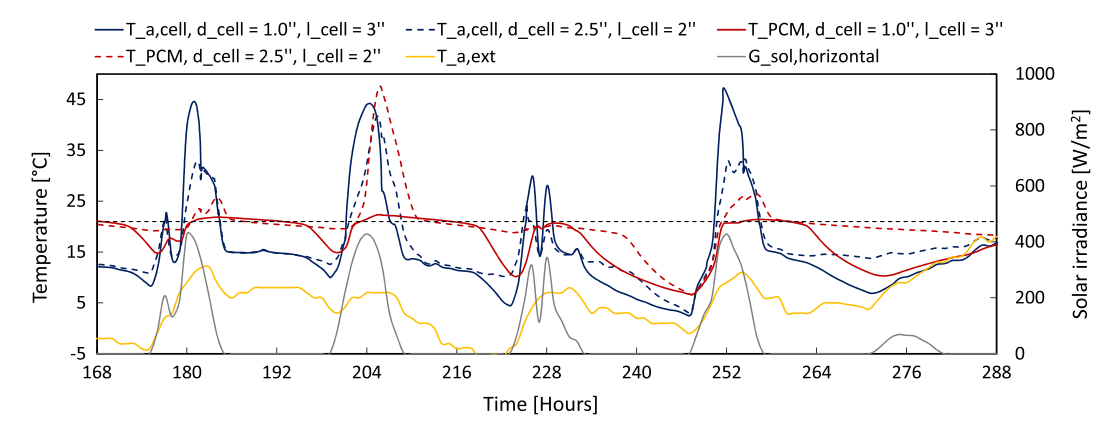


Fig. 9. PCM temperature (TC 2, see Fig. 5) for both experiment and numerical simulation, for  $d_{cell} = 25 \text{ mm } (1'')$  and 38 mm (1.5'').



**Fig. 10.** Comparison between the use of an external cover with and without a ITO and an AR coating, for the **winter** test period. A significant enhancement in heat loss can be observed with the use of these coatings. The cumulative heat loss decreases from 6.4 to 3.6 MJ for the winter period simulated.



**Fig. 11.** Average air cell temperature,  $T_{a,cell}$ , and PCM temperature,  $T_{pcm}$ , for opposite end cell aspect ratios ( $l_{cell}/d_{cell}$ ). More energy harvesting occurs in the case of the larger cell diameters. This stabilizes winter interior surface temperatures closer to the comfort temperature, reducing heat loss.

# 5.2. Introduction of ITO and AR coatings

The baseline can be improved by changing the optical characteristics of the external cover. An ITO coating can be applied on the exterior side of the system, combined with an AR coating on the internal side of the exterior cover. According to (Giovannetti et al., 2012), this decreases the emissivity,  $\varepsilon$ , of the external system surface from 0.84 to 0.20. A drawback, however, is a slight increase in the reflection of solar radiation, which increases from 0.09 to 0.13 for radiation normal to the surface. Fig. 10 presents a comparison of the average PCM temperature between the system with and without these coatings. The average PCM temperature increases from 19.4 °C to 21.5 °C, net heat loss decreases from 6.4 to 3.6 MJ, for the winter period simulated. A solid to liquid phase transition is completed more easily, and, as a consequence, liquid to solid phase transitions are completed less frequently. This allows for a more efficient bridging of cycles with low levels of solar irradiance.

# 5.3. Phase transition

The phase transition temperature,  $T_{pc}$ , lies best as close to the interior comfort temperature (20–22 °C). A higher  $T_{pc}$  would merely lead to an increase in heat loss during winter conditions. A lower  $T_{pc}$  would lead to a continuous heat flux from the building interior to the PCM, which again, increases the overall heat loss.

# 5.4. Cell dimensions/ratio

The most important aspect of the system is the air cell size ratio  $(l_{cell}/d_{cell})$  because this influences both the thermal resistance of the air cell and the absorption of solar irradiance. A combination of different values for  $l_{cell}$  (51 mm (2") to 76 mm (3")) and  $d_{cell}$  (13 mm (0.5") to 64 mm (2.5")) have been evaluated for winter conditions. Typical average air cell and PCM temperature diurnal cycles for opposite end cell aspect ratios are presented in Fig. 11.

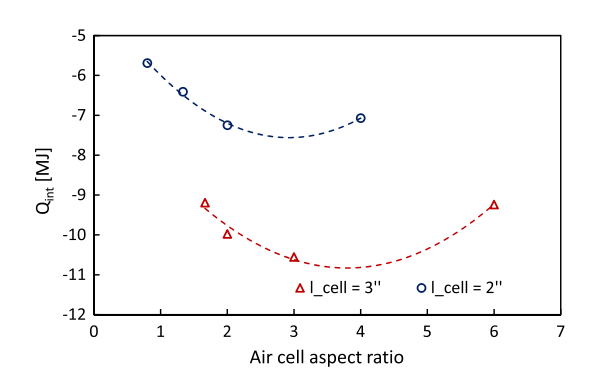


**Fig. 12.** The net heat exchange across the building envelope, for the **winter** test period, as a function of cell size ratio ( $l_{cell}/d_{cell}$ ). The highest levels of winter energy harvesting are generated with large cell diameters and relatively short air cells. Within the air cell, it appears more favorable view factors outweigh the significance of suppressed internal convective heat transfer.

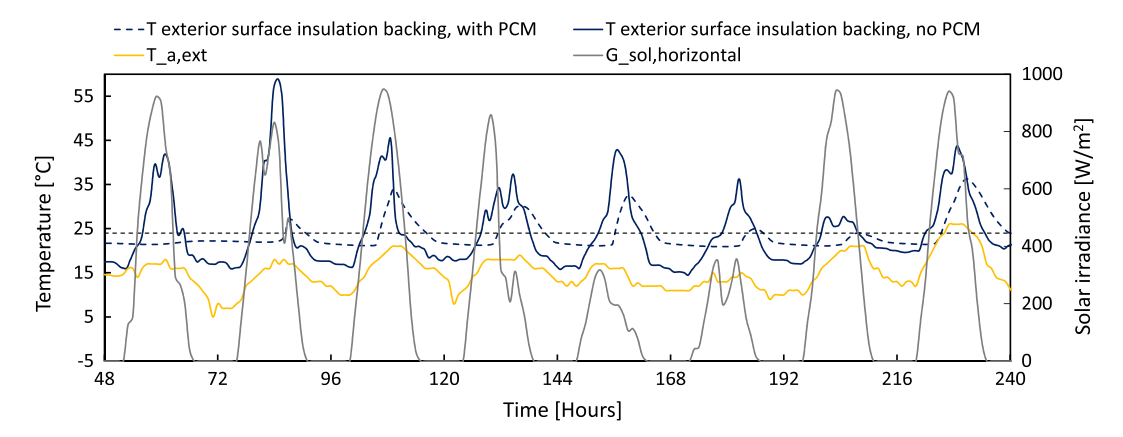


**Fig. 13.** Temperature on the exterior surface of the insulation backing with and without the 25 mm (1") layer of PCM, for the **summer** test period ( $l_{cell} = 51 \text{ mm} (2") d_{cell} = 38 \text{ mm} (1.5")$ ). Temperature peaks appear suppressed due to phase transitions. Night cycles are not able to solidify the PCM, allowing for a potential increase in efficiency.

Here, large cell diameters, or small cell aspect ratios, appear to exhibit a continuously higher average PCM temperature. This is due to a more favorable view factor situation, allowing for more solar radiation to be absorbed at the absorber wall. In fact, only the PCM in the 64 mm (2.5") diameter cell is able to fully complete phase transitions. As a consequence, the net heat loss decreases significantly from 10.6 MJ ( $d_{cell}=25~{\rm mm}~(1.0"), l_{cell}=76~{\rm mm}~(3.0"))$  to 5.7 MJ ( $d_{cell}=64~{\rm mm}~(2.5"), l_{cell}=51~{\rm mm}~(2.0"))$  over the winter test period.

However, when the cell aspect ratio becomes small enough, the natural convection flow within the air cell will be suppressed almost completely (Edwards and Catton, 1969). This explains why winter air cell temperatures tend to be higher from sunrise to sunset for smaller air cell diameters or larger air cell aspect ratios (see Fig. 11). In Fig. 12, the net heat exchange for the time period simulated is plotted as a function of the air cell aspect ratio for both a 51 mm (2") and a 76 mm (3") cell length. Here, it becomes clear that small enough cell diameters also lead to reduced winter heat losses. Therefore, both a small and a large air cell aspect ratio have the ability for a similar reduction in winter heat losses. For  $l_{cell} = 76 \text{ mm } (3'')$ , both a 1.7 and 6.0 cell aspect ratio exhibit a 9.2 MJ net heat loss over the winter test period. A maximum heat loss, on the other hand, is reached at a cell aspect ratio of about 3-4 (10.6 MJ). For a smaller cell length (Fig. 12,  $l_{cell} = 51 \text{ mm } (2'')$ ), the solar energy harvesting phenomenon appears to become dominant, as a shorter cell length leads to viewfactors that favor solar energy harvesting, lifting the curve in Fig. 12. This allows for a net winter heat loss of as low as 6.1 MJ.

The danger of the proposed system is potential overheating during summer conditions. In Fig. 13 a comparison is made between the system with and without a 25 mm(1") layer of PCM. The PCM leads to a significant reduction in heat gains over the summer test period, from 10.6 MJ to 6.2 MJ. A 42% reduction in net heat gains could potentially lead to viability of the system across the year for a four season climate. This reduction happens despite of higher PCM temperature during night cycles in the case with PCM. The PCM is, therefore, not able to completely solidify during night cooling, allowing for an increase in efficiency still.

## 6. Discussion

The system, as proposed, inherently contains a balance between the ability to harvest solar energy and the ability to prevent heat exchange. This balance becomes clear when investigating the influence of the cell size aspect ratio. Cells with a small aspect ratio allow for significant solar energy harvesting, although these could lead to excess energy gains in summer and excess energy losses during periods with prolonged solar irradiance. Cells with very large cell aspect ratio's, on the other hand have the ability to prevent heat exchange due to the suppression of internal convection, although these do not make efficient use of the solar irradiance available. The geometric design of the air cell appears to exhibit a global maximum of winter heat losses at a cell aspect ratio of about 3–4 for a cell length of 76 mm (3") and about 2–3 for a cell length of 51 mm (2"). This, however, changes when applying coatings to the external transparent front cover.

In order to allow for efficient collection of energy harvesting, thus keeping a small cell aspect ratio, control mechanisms have been introduced to prevent excess heat gains or losses. To begin with, opaque walls are introduced in between the individual air cells, allowing solar irradiance to reach the absorber wall directly during winter (small incidence angles), yet mainly indirectly during summer (large incidence angles), lowering summer temperature peaks. The addition of a layer of PCM behind the absorber surface allows for the buffering of heat energy, which increases both summer and winter performance of the system. A 25 mm (1") layer of PCM with a latent heat capacity of 180 kg appears to reduce summer heat gains by 42%.

The application of exotic coatings, which maintain a high transmission of solar radiation across the front cover and reduce the emissivity of the exterior surface, increase the winter heat gains significantly. Although it remains to be seen whether or not this increases the annual performance, as it could increase summer temperatures excessively. An optimum design will, of course, dependent on location and building envelope orientation, with a specific heating and cooling seasons lengths and severity.

#### 7. Conclusion

The system, as proposed in this paper, does behave as expected. It is, however, not yet fully optimized to function as intended throughout a full year. The numerical framework, which is validated in this paper, can be used to further improve and optimize the system. The numerical model and results presented shed some light on how the system can be improved and what the limitations of these improvements probably are.

 During winter conditions, both a small and large cell aspect ratio is able to reduce net heat energy loss. A small cell aspect ratio improves solar energy harvesting significantly, allowing

- for significant reduction in winter net heat energy losses in combination with PCM. For a cell length of 76 mm (3''), a maximum heat loss seems to occurs at a cell aspect ratio of about 3–4.
- The addition of PCM behind the air cell increases system efficiency in both summer and winter conditions. Summer heat gains seem reducible up to 42% by the addition of PCM.
- State-of-the-art coatings, on the other hand, have ability to improve the energy harvesting potential during winter conditions, although these could very well..... lead to excess heat gains during summer conditions.

Many aspects of the proposed system, however, do require further investigation. Any optimized design solution will be a function of orientation and location, and will inherently be a trade-off between winter and summer demands.

Further research will explore many potential solutions that optimize the design to perform better across the year in a four season climate. The system might require some dynamic response to work better in both winter and summer conditions, although the goal is to keep the control systems passive. The application of thermochromic or electrochromic materials, for example, may also be used to regulate the intake of heat energy caused by solar irradiance. A combination of approaches will likely be required to accommodate self-regulation for a wide range of climate situations. It will also be required to evaluate the system in a whole building energy modeling environment. This will capture the complete behavior of the system, even when applied only on southern oriented façades.

#### Acknowledgements

Support from the National Science Foundation, award number CMMI-1662903 & 1662675, Directorate for Engineering, Division of Civil, Mechanical and Manufacturing Innovation (CMMI), Structural and Architectural Engineering and Materials program (SAEM), is much appreciated.

# References

- Al-Mahdouri, A., Gonome, H., Okajima, J., Maruyama, S., 2014. Theoretical and experimental study of solar thermal performance of different greenhouse cladding materials. Sol. Energy 107, 314–327.
- Baetens, R., Jelle, B.P., Gustavsen, A., 2010. Phase change materials for building applications: a state-of-the-art review. Energy Build. 42, 1361–1368.
- Bergman, T.L., Lavine, A.S., Incropera, F.P., Dewitt, D.P., 2011. Fundamentals of Heat and Mass Transfer. Wiley and Sons, Inc., New York.
- Berry, J., Michaels, J., 2012. Annual Energy Review 2011. U.S. Energy Information Administration, Office of Energy Statistics.
- Boukhris, Y., Gharbi, L., Ghrab-Morcos, N., 2009. Phase change materials for building applications: a state-of-the-art review. Build. Simul. 2, 1996–3599.
- Buker, M.S., Riffat, S.B., 2015. Building integrated solar thermal collectors a review. Renew. Sustain. Energy Rev. 51, 327–346.
- Cabeza, L.F., Castell, A., Barreneche, C., de Gracia, A., Fernndez, A.I., 2011. Materials used as PCM in thermal energy storage in buildings: a review. Renew. Sustain. Energy Rev. 15, 1675–1695.
- Cadafalch, J., Cònsul, R., 2014. Detailed modelling of flat plate solar thermal collectors with honeycomb-like transparent insulation. Sol. Energy 107, 202– 209.
- Chan, H.Y., Riffat, S.B., Zhu, J., 2010. Review of passive solar heating and cooling technologies. Renew. Sustain. Energy Rev. 14, 781–789.
- Chen, D., 2001. Anti-reflection (AR) coatings made by sol-gel processes: a review. Sol. Energy Mater. Sol. Cells 68, 313–336.
- Clark, G., Allen, C., 1978. The estimation of atmospheric radiation for clear and cloudy skies. In: Proceedings of the 2nd National Passive Solar Conference (AS/ ISES), 16–18 March 1978, University of Pennsylvania, pp. 675–678.
- Cuce, E., Riffat, S.B., 2015. A state-of-the-art review on innovative glazing technologies. Renew. Sustain. Energy Rev. 41, 695–714.
- de Gracia, A., Navarro, L., Castell, A., Cabeza, L.F., 2015. Energy performance of a ventilated double skin facade with PCM under different climates. Energy Build. 91, 37–42.
- Ebisawa, J., Ando, E., 1998. Solar control coating on glass. Curr. Opin. Solid State Mater. Sci. 3, 386–390.

- Edwards, D.K., Catton, I., 1969. Prediction of heat transfer by natural convection in closed cylinders heated from below. Int. J. Heat Mass Transf. 12, 23–30.
- Emel, M., Abadie, M., Mendes, N., 2007. New external convective heat transfer coefficient correlations for isolated low-rise buildings. Energy Build. 39, 335– 342.
- Fallahi, A., Haghighat, F., Elsadi, H., 2010. Energy performance assessment of double-skin façade with thermal mass. Energy Build. 42, 1499–1509.
- Francia, G., 1961. A new collector of solar radiant energy: theory and experimental verification. Paper presented at the United Nations Conference on New Sources of Energy, Rome.
- Giovannetti, F., Föste, S., Ehrmann, N., Rockendorf, G., 2012. High transmittance, low emissivity glass covers for flat plate collectors: applications and performance. Energy Procedia 30, 106–115.
- Gratia, E., De Herde, A., 2004. Natural cooling strategies efficiency in an office building with a double-skin façade. Energy Build. 36, 1139–1152.
- Hammarberg, E., Roos, A., 2003. Antireflection treatment of low-emitting glazings for energy efficient windows with high visible transmittance. Thin Solid Films 442, 222–226.
- Hordeski, M.F., 2004. Dictionary of Energy Efficiency Technologies. Fairmont Press, Inc., Lilburn, GA.
- Howell, J.R., Mengüç, M.P., Siegel, R., 2016. Thermal Radiation Heat Transfer. Taylor and Francis Group, LLC, Florida
- Hutcheon, N.B., Handegord, G.O.P., 1995. Building Science for a Cold Climate. National Research Council of Canada, Montreal.
- Jones, H.R.N., 2000. Radiation Heat Transfer. Oxford University Press, Oxford.
- Judkoff, R.D., Neymark, J.S., 1995. Building Energy Simulation Test (BESTEST) and Diagnostic Method. National Renewable Energy Laboratory, Colorado.
- Kaushika, N.D., Sumathy, K., 2003. Solar transparent insulation materials: a review. Renew. Sustain. Energy Rev. 7, 317–351.
- Kruzner, K., Cox, K., Machmer, B., Klotz, L., 2013. Solar transparent insulation materials: a review. Energy Policy 55, 82–94.
- Kuznik, F., Damien, D., Johannes, K., Roux, J.J., 2011. A review on phase change materials integrated in building walls. Renew. Sustain. Energy Rev. 15, 379–301
- Lai, C.M., Hokoi, S., 2015. Solar façades: a review. Build. Environ. 91, 152-165.
- Lawrence, M.G., 2005. The relationship between relative humidity and the dewpoint temperature in moist air: a simple conversion and applications. Bull. Am. Meteorol. Soc. 86, 225–233.
- Ma, T., Yang, H., Zhang, Y., Lu, L., Wang, X., 2015. Using phase change materials in photovoltaic systems for thermal regulation and electrical efficiency improvement: a review and outlook. Renew. Sustain. Energy Rev. 43, 1273– 1284.
- Meeus, J., 1991. Astronomical Algorithms. Willmann-Bell, Inc., Richmond, Virginia. Min, T.C., Schutrum, L.F., Parmelee, G.V., Vouris, J.D., 1956. Natural convection and radiation in a panel heated room. Heat. Pip. Air Cond. (May), 153–160
- Onbasioglu, H., Egrican, A.N., 2002. Experimental approach to the thermal response of passive systems. Energy Convers. Manage, 43, 2053–2065.
- Perez, R.S., Seals, R., Ineichen, P., Stewart, R., Menicucci, D., 1987. A new simplified version of the Perez diffuse irradiance model for tilted surfaces. Sol. Energy 39, 221–231.
- Perez, R., Stewart, R., Seals, R., Guertin, T., 1988. The Development and Verification of the Perez Diffuse Radiation Model. Atmospheric Sciences Research Center.
- Perez, R.R., Ineichen, P., Maxwell, E.L., Seals, R.D., Zelenka, A., 1992. Dynamic global-to-direct irradiance conversion model (ASHRAE). ASHRAE Trans. 98, 3578–3595.
- Quesada, G., Rousse, D., Dutil, Y., Badache, M., Hall, S., 2012a. A comprehensive review of solar facades. Opaque solar facades. Renew. Sustain. Energy Rev. 16, 2820–2832.
- Quesada, G., Rousse, D., Dutil, Y., Badache, M., Hall, S., 2012b. A comprehensive review of solar facades. Transparent and translucent solar facades. Renew. Sustain. Energy Rev. 16, 2643–2651.
- Quimby, R.S., 2006. Photonics and Lasers. John Wiley and Sons, Inc., Worcester, Massachusetts.
- Ralegaonkar, R.V., Gupta, R., 2010. Review of intelligent building construction: a passive solar architecture approach. Renew. Sustain. Energy Rev. 14, 2238–2242
- Rosencrantz, T., Bulowhube, H., Karlsson, B., Roos, A., 2005. Increased solar energy and daylight utilisation using anti-reflective coatings in energy-efficient windows. Sol. Energy Mater. Sol. Cells 89, 249–260.
- Saadatian, O., Sopian, K., Lim, C.H., Asim, N., Sulaiman, M.Y., 2012. Trombe walls: a review of opportunities and challenges in research and development. Renew. Sustain. Energy Rev. 16, 6340–6351.
- Sadineni, S.B., Madala, S., Boehm, R.F., 2011. Passive building energy savings: a review of building envelope components. Renew. Sustain. Energy Rev. 15, 3617–3631.
- Samuel, L.D.G., Nagendra, S.S.M., Maiya, M.P., 2013. Passive alternatives to mechanical air conditioning of building: a review. Build. Environ. 66, 54–64.
- Schaefer, C., Bruer, G., Szczyrbowski, J., 1997. Low emissivity coatings on architectural glass. Surf. Coat. Technol. 93, 37–45.
- Shameri, M.A., Aİghoul, M.A., Sopian, K., Zain, M., Fauzi, M., Elayeb, O., 2011. Perspectives of double skin façade systems in buildings and energy saving. Renew. Sustain. Energy Rev. 15, 1468–1475.
- Sharma, M.S., Kaushika, N.D., 1987. Design and performance characteristics of honeycomb solar pond. Energy Convers. Manage. 27, 111–116.

- Shen, J., Lassue, S., Zalewski, L., Huang, D., 2007. Numerical study on thermal behavior of classical or composite Trombe solar walls. Energy Build. 39, 962–974.
- Stevanovi, S., 2013. Optimization of passive solar design strategies: a review. Renew. Sustain. Energy Rev. 25, 177–196.
- Tatsidjodoung, P., Le Pierrs, N., Luo, L., 2013. A review of potential materials for thermal energy storage in building applications. Renew. Sustain. Energy Rev. 18, 327–349.
- Veinberg, B.P., Veinberg, V.B., 1959. Optics in Equipment for the Utilization of Solar Energy (English translation). A Review of Potential Materials for Thermal Energy Storage in Building Applications. State Publishing House of Defense Industry.
- Wallner, G.M., Platzer, W., Lang, R.W., 2005a. Structure-property correlations of polymeric films for transparent insulation wall applications. Part 1: solar optical properties. Sol. Energy 79, 583–592.
- Wallner, G.M., Platzer, W., Lang, R.W., 2005b. Structure-property correlations of polymeric films for transparent insulation wall applications. Part 2: infrared optical properties. Sol. Energy 79, 593–602.
- Wallner, G.M., Hausner, R., Hegedys, H., Schobermayr, H., Lang, R.W., 2006. Application demonstration and performance of a cellulose triacetate polymer film based transparent insulation wall heating system. Sol. Energy 80, 1410– 1416.
- Walton, G.N., 1983. Thermal Analysis Research Program Reference Manual. National Bureau of Standards.
- Zamora, B., Kaiser, A.S., 2009. Thermal and dynamic optimization of the convective flow in Trombe Wall shaped channels by numerical investigation. Heat Mass Transf. 45, 1393–1407.